


PAPER

 View Article Online
 View Journal | View Issue
Cite this: *Nanoscale*, 2023, **15**, 13628

All-inorganic Mn^{2+} -doped metal halide perovskite crystals for the late-time detection of X-ray afterglow imaging†

Sijian Wu,^a Lifang Yuan,^b Geng Chen,^a Chaoyue Peng^a and Yahong Jin  ^{*,a}

All-inorganic metal halide perovskite (MHP) materials have been widely studied because of their unique optoelectronic properties, whereas there has been little research reported on their X-ray afterglow imaging properties. Herein, we report the design and synthesis of Mn^{2+} -doped hexagonal CsCdCl_3 MHP crystals with excellent X-ray scintillation and X-ray induced afterglow. The orange emission from Mn^{2+} shows a red shift due to the strong interaction of the Mn^{2+} – Mn^{2+} dimers formed at higher doping concentrations. The high-energy X-rays with higher electron filling capacity to feed the shallow (0.71 eV) and deep (0.90–1.08 eV) traps enable a long orange afterglow for more than 300 min. The afterglow emission can be rejuvenated effectively by 870 nm stimulus or heating even after 72 h of decay. Finally, we demonstrate the proof-of-concept applications of the fabricated flexible scintillator films for real-time online X-ray imaging with a spatial resolution of 12.2 lp mm^{-1} , as well as time-lapse X-ray imaging recorded by a cell phone, which shows promise for being able to do offline late-time detection of X-ray afterglow imaging in the future.

 Received 12th May 2023,
 Accepted 20th July 2023
 DOI: 10.1039/d3nr02208k
 rsc.li/nanoscale

1. Introduction

Scintillators, defined as a type of material with the ability to absorb high-energy ionising radiation and then convert it into low-energy visible photons *via* radioluminescence (RL), have gained significant interest due to their ability to facilitate the detection and measurement of radiation, making them invaluable in widespread applications, such as non-destructive inspection, medical radiography and diagnosis, radiation safety monitoring, and nuclear cameras.^{1–3} Traditional scintillators, such as Tl^+ -doped $\text{Cs}(\text{Na})\text{I}$, $\text{Bi}_4\text{Ge}_3\text{O}_{12}$, and Ce^{3+} -doped YAlO_3 , have demonstrated remarkable scintillation properties.^{4–7} However, the high-temperature manufacturing process of these materials presents significant cost and implementation challenges. Moreover, the resultant powdered scintillator is prone to severe aggregation, impeding its seamless integration into device architectures. Thus, the development of low-cost, solution-processable scintillators with high

X-ray sensitivity, prepared *via* low-temperature methods, has become increasingly necessary.

Metal halide perovskites (MHPs) are known as a class of superstar semiconductors, and have become a prime candidate for use as scintillators in recent years, because of their advantages of exceptional stopping power, high sensitivity to X-rays, large light yield, and easy preparation. Typically, some organic–inorganic hybrid and all-inorganic MHPs, such as $(\text{DIET})_3\text{Cu}_3\text{X}_3$,⁸ $(\text{BA})_2\text{CsAgBiBr}_7$,⁹ $[\text{TPPen}]_2\text{MnBr}_4$,¹⁰ $\text{TPP}_2\text{MnBr}_4$,¹¹ CsPbX_3 ,^{12–14} Rb_2CuBr_3 ,¹⁵ $\text{Cs}_3\text{Cu}_2\text{X}_5$,^{16,17} Cs_2AgI_3 , Cu ,¹⁸ and Cs_2ZrCl_6 ,¹⁹ have been reported and demonstrated for use in ultrasensitive X-ray detectors and low-dose X-ray imaging devices. Despite tremendous efforts, the vast majority of studies have focused on real-time X-ray imaging for flat objects by virtue of their outstanding scintillation properties, while ignoring time-lapse X-ray imaging due to the lack of efficient afterglow MHPs.^{20–22} Afterglow, a captivating phenomenon where a material can store light energy by capturing the electrons and/or holes, and then releasing them continuously at room temperature (RT) in the form of a self-sustained photon emission,^{23–28} is commonly considered to be detrimental to a high-quality scintillator and needs to be avoided in practical applications. However, the utilization of afterglow in MHP scintillators offers incomparable merits, particularly for time-lapse offline X-ray imaging of curved objects, and long-term storage X-ray imaging in some harsh environments.^{29,30} Fortunately, Zheng *et al.* made a pioneering

^aSchool of Physics and Optoelectronic Engineering, Guangdong University of Technology, WaiHuan Xi Road, No. 100, Guangzhou 510006, PR China.
E-mail: yhj@gdut.edu.cn

^bSchool of Electronics and Communications, Guangdong Mechanical & Electrical Polytechnic, Guangzhou 510515, PR China

† Electronic supplementary information (ESI) available. See DOI: <https://doi.org/10.1039/d3nr02208k>

contribution to the synthesis and study of all-inorganic lead-free MHPs with excellent afterglow properties, such as Mn^{2+} -doped double perovskite alloys of $\text{Cs}_2\text{Na}_x\text{Ag}_{1-x}\text{InCl}_6$ showing a red afterglow,³¹ and a Tb^{3+} -doped double perovskite of $\text{Cs}_2\text{NaScCl}_6$ exhibiting an intense green afterglow for up to 12 h.³² These compelling results inspired us to further explore the all-inorganic lead-free afterglow MHPs and extend their applications to time-lapse offline X-ray imaging.

In this work, we reported on the Mn^{2+} -doped all-inorganic metal halide crystals that combined scintillation and long afterglow properties. Hexagonal cadmium-based MHP crystals were prepared and deliberate doping with Mn^{2+} ions not only boosted the original photoluminescent (PL) intensity up to 11.3 times, but also prolonged the X-ray induced orange afterglow for up to 300 min. The structure (including crystal structure and defects)-property relationships (including PL, afterglow, optically stimulated luminescence (OSL), and scintillation properties) and electron dynamics were systematically studied using the steady-state and transient fluorescence, thermoluminescence, and radioluminescence. Because of the exceptional X-ray absorption capacity and long afterglow characteristics, the resulting phosphors were utilized to produce flexible scintillator films, demonstrating real-time online X-ray imaging with spatial resolution of 12.2 lp mm^{-1} , together with the extension of the application for offline time-lapse X-ray imaging.

2. Experimental section

2.1. Materials

The raw materials of caesium chloride (CsCl , Aladdin, 99.99%), cadmium chloride (CdCl_2 , Macklin, 99.99%), manganese carbonate (MnCO_3 , Aladdin, 99.95%), hydrochloric acid (HCl , Guangzhou Chemical Reagent Factory, China, 37 wt% in water), and anhydrous ethanol ($\text{CH}_3\text{CH}_2\text{OH}$, Guangzhou Chemical Reagent Factory, China, AR) were used as received without any further purification.

2.2. Synthesis of $\text{CsCdCl}_3\text{:Mn}^{2+}$ crystal

The Mn^{2+} -doped CsCdCl_3 perovskite (CCCP) crystals were synthesized using a hydrothermal method with a stoichiometric ratio of CCCP:x\%Mn^{2+} . In a typical synthesis, 1 mmol of CsCl , $1 - x$ mmol of CdCl_2 , and x mmol of MnCO_3 were dissolved in 5 ml of HCl and then transferred to a 25 ml Teflon autoclave. The mixture was heated up to 180°C , held for 24 h, and then slowly cooled to RT over 5 h. Finally, the as-synthesized sample was washed three times with anhydrous $\text{CH}_3\text{CH}_2\text{OH}$ and then dried at 60°C overnight before further measurements were carried out.

2.3. Fabrication of the CCCP: Mn^{2+} films

The gel precursor was prepared by mixing PDMS with the curing agent (10:1 by mass). Then, the as-obtained CCCP: Mn^{2+} powder was added into the gel precursor (1:7 by mass) with vigorously stirring. Subsequently, the mixture was poured

into a mould made from a circular aluminium alloy plate. The resulting composites were finally heated at 80°C for 4 h. After cooling down to RT, the as-fabricated film with a thickness of $\sim 1.5 \text{ mm}$ was peeled from the mould and used for the X-ray imaging.

2.4. Measurement and characterization

The powder X-ray diffraction (XRD) spectra of the crystals were collected using a Bruker D8 ADVANCE diffractometer equipped with a $\text{CuK}\alpha$ X-ray tube operating at 50 kV and 60 mA. The morphology and energy dispersive X-ray spectroscopy characterization were measured using SEM with a Tescan LYRA3 instrument, and energy-dispersive X-ray spectroscopy mapping (EDS-mapping) was carried out at an acceleration voltage of 10 kV with a charge coupled device camera. Diffuse reflectance spectra were obtained using UV-vis-NIR spectrophotometry with a Shimadzu UV-3600 plus. Photoluminescence excitation (PLE), PL spectra, fluorescence decay curves, and afterglow decay profiles were collected using fluorescence spectrometry with Edinburgh Instruments FLS980, with a continuous 450 W xenon lamp (Osram). Photoluminescence quantum efficiency (PLQY) was measured by a quantum yield measurement system with a Hamamatsu Quantaurus-QY Plus C13534-31. The thermoluminescence (TL) and OSL were collected using thermoluminescence dosimetry with a Risø TL/OSL-DA-20 instrument from RT to 400°C with a heating rate of 3°C s^{-1} . A commercially available X-ray tube, Moxtek, TUB00154-9I-W06 with maximum power of 12 W was utilized for the measurements of radioluminescence (RL) and time-lapse X-ray imaging. The X-ray tube voltage and working current were set at 60 kV and 150 μA , respectively. The X-ray images were recorded using a general digital camera or a 12 megapixel rear camera on an iPhone 12 after being reflected by a reflector without an extra attenuator.

3. Results and discussion

As shown in Fig. 1a, the XRD patterns of the samples of CCCP: $x\%\text{Mn}$ ($x = 0\text{--}30$) match well with the standard XRD pattern (PDF#70-1615) without any impurity phase, indicating the good phase purity of the products before and after Mn^{2+} doping. Fig. 1b shows the crystal structure of CCCP, which indicates a hexagonal system with a $P6_3/mmc$ space group. Apparently, there are two kinds of Cd sites in the 3D crystal structure. One is coordinated by six Cl atoms, forming $[\text{Cd}_1\text{Cl}_6]$ octahedrons. Two Cd2 are coordinated with nine Cl to form a $[\text{Cd}_2\text{Cl}_9]$ subunit, which is constructed from face-sharing $[\text{Cd}_2\text{Cl}_6]$ octahedrons. The $[\text{Cd}_2\text{Cl}_9]$ dimers corner-shared with the $[\text{Cd}_1\text{Cl}_6]$ octahedrons. Consequently, the Mn^{2+} ions enter either into Cd1 or Cd2 sites, and the Mn^{2+} - Mn^{2+} dimers are prone to be formed because of the superexchange coupled energy levels of two adjacent Mn^{2+} ions in $[\text{Cd}_2\text{Cl}_9]$ with a distance of 3.33 \AA ($< 5 \text{ \AA}$).³³ To reveal this, we focussed on the shift of the strongest (110) and the second strongest (204) XRD peaks. As shown in Fig. 1c, as the Mn^{2+} doping con-

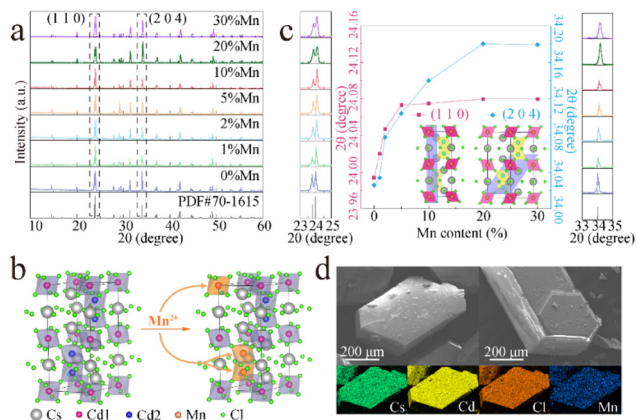


Fig. 1 (a) The XRD patterns of CCCP: $x\%$ Mn crystals (left) and magnified images of the (204) diffraction peaks (right). (b) The crystal structure of CCCP and the doping of Mn^{2+} into two different Cd sites. (c) The XRD peaks corresponding to the (110) and (204) planes of the Mn^{2+} -doped CsCdCl_3 perovskite (CCCP) and angle shifts as the function of Mn^{2+} doping concentration. (d) The SEM images and EDS elemental mapping of the CCCP:5%Mn $^{2+}$ crystals.

centration increases, the diffraction peaks shift continuously and slightly towards higher angles. According to Bragg's law of $2d \sin \theta = n\lambda$ and the similarity-intermiscibility theory, this change is attributed to the substitution of smaller Mn^{2+} ($r = 0.83 \text{ \AA}$, CN = 6) for Cd^{2+} ($r = 0.95 \text{ \AA}$, CN = 6) rather than Cs^+ ($r = 1.67 \text{ \AA}$, CN = 6),³⁴ which further verifies the successful incorporation of Mn^{2+} into the CCCP host lattice. Remarkably, the XRD peak of the (110) plane presents a much faster angle shift rate than that of the (204) plane at a low Mn^{2+} doping concentration ($x < 1$) and a similar angle shift rate at $1 < x < 5$. When x is larger than 5, the XRD peak of the (110) plane remains almost invariant whereas the (204) plane further shifts, notably to higher angle until $x = 20$. From the insets of Fig. 1c, it can be seen that the (110) and (204) planes are mainly related to Cd1 and Cd2, respectively. Thus, it can be concluded that Mn^{2+} preferentially enters into the Cd1 sites at a low doping concentration, and then into the Cd2 sites at a higher doping concentration. The SEM images and elemental mapping of the CCCP:5%Mn sample shown in Fig. 1d show the hexagonal bulk crystals with the uniformly distributed Cd, Cl, Cs, and Mn elements.

Fig. 2a shows the UV-vis diffuse reflectance spectra of the CCCP: $x\%$ Mn ($x = 0$ –20) crystals. The reflectivity of the CCCP host shows a plateau in the wavelength range of 270–800 nm and starts to decrease sharply at 270 nm which is caused by host absorption. In contrast, a notable drop in the wavelength range of 240–330 nm and multiple absorption peaks in the wavelength range of 340–500 nm appear for the Mn^{2+} -doped ones, which are typically caused by charge transfer and d–d transitions of Mn^{2+} ions, respectively.³⁵ In addition, the Kubelka–Munk function and the Tauc relationship were used to estimate the optical bandgap according to the following function:³⁶

$$(F(R)h\nu)^{1/n} = A(h\nu - E_g) \quad (1)$$

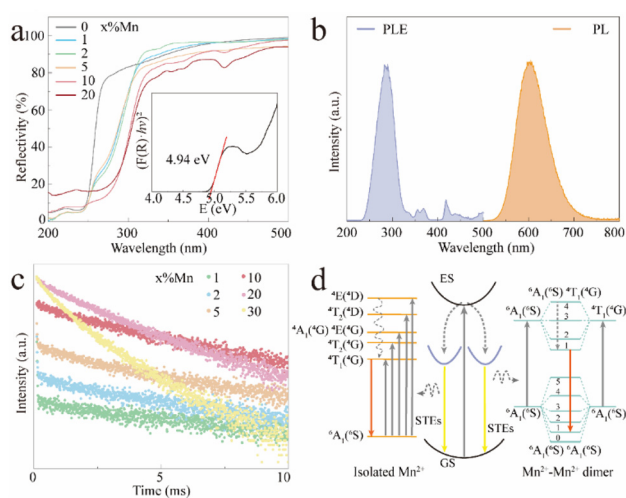


Fig. 2 (a) Diffuse reflectance spectra of CCCP: $x\%$ Mn crystals and the plot of $(F(R)h\nu)^2$ versus the light energy $h\nu$ (inset). (b) Excitation and emission spectra of the CCCP:10%Mn crystals. (c) The fluorescence decay curve of the CCCP: $x\%$ Mn crystals ($\lambda_{\text{ex}} = 290 \text{ nm}$, $\lambda_{\text{em}} = 605 \text{ nm}$). (d) Schematic diagram for the photophysical processes in CCCP:Mn crystals.

where $F(R)$ is the reflectance coefficient, $h\nu$ is the photon energy, A is the proportional constant, and E_g is the optical bandgap. Herein, $n = 1/2$ is adopted for the estimations because of the direct bandgap of CCCP.³⁷ The optical bandgap of CCCP was calculated to be 4.94 eV. Fig. S1 (ESI)[†] shows the PLE and PL spectra of the non-doped CCCP crystals. The PLE spectrum shows a narrow peak with the maximum at 255 nm. Upon 255 nm excitation, it exhibits orange emission with a broad band centred at 598 nm in the wavelength range of 530–750 nm. Such a large Stokes' shift of the broadband emission for CCCP was consistent with the characteristics of self-trapped exciton (STE) emission.^{38,39} As shown in Fig. 2b, the Mn^{2+} -doped CCCP crystals exhibit a significantly different PLE spectrum and a much brighter PL emission with the peak maximum at 605 nm. The PLQY was found to be about 80%. Compared with the non-doped one, the PLE spectra of the Mn^{2+} -doped CCCP showed a noticeable red shift to 290 nm (Fig. S2, ESI)[†], which was attributed to the overlap of the STE excitation and the charge transfer transitions. In addition, according to the Tanabe–Sugano diagram shown in Fig. S3 (ESI)[†], some new PLE peaks within 340–450 nm were ascribed to characteristic d–d transitions of the Mn^{2+} ions, i.e., from $^6\text{A}_{1g}$ to $^4\text{E}_g$ (D) (335 nm), $^4\text{T}_{2g}$ (D) (355 nm), $^4\text{A}_{1g}$, $^4\text{E}_g$ (D) (369 nm), $^4\text{T}_{2g}$ (G) (419 nm), and $^4\text{T}_{1g}$ (G) (442 nm). Meanwhile, the PL spectra present a slight red shift (Fig. S2, ESI)[†] due to the $^4\text{T}_{1g}$ – $^6\text{A}_{1g}$ energy level transitions of Mn^{2+} .^{40–42} As the Mn^{2+} doping concentration increased, it showed further red shifting caused by the formation of the Mn^{2+} – Mn^{2+} dimers, and resulted in stronger interactions between them.^{43,44} Moreover, the orange emission intensity reached the maximum which was about 11.3 times higher than the undoped one at $x = 10\%$ and then decreased due to concentration quenching.

To further explore the fluorescence dynamics of the different emission centres, the fluorescence decay behaviour at RT was investigated. All the luminescence decay curves were well fitted with the following bi-exponential decay function (2):^{45,46}

$$I_t = A_1 \exp\left(-\frac{t}{\tau_1}\right) + A_2 \exp\left(-\frac{t}{\tau_2}\right) \quad (2)$$

where I_t is the luminescence intensity, t is time, A_1 and A_2 are two constants, and τ_1 and τ_2 are the lifetimes for the two exponential components. The average lifetime (τ) can be calculated by the formula: $\tau = \frac{A_1\tau_1^2 + A_2\tau_2^2}{A_1\tau_1 + A_2\tau_2}$. As shown in Fig. S4 (ESI),† the average lifetime of undoped CCCP was calculated to be 4.0 μ s. In contrast, as shown in Fig. 2c, the average lifetimes of the CCCP: $x\%$ Mn²⁺ ($x = 1$ –30) crystals, equalling 10.22, 7.92, 5.43, 5.07, 3.08 and 1.47 ms, were much slower due to the spin-forbidden 3d–3d transition nature of the Mn²⁺ ions. The monotonous decrease of lifetime with the increase of Mn²⁺ doping content might be ascribed to the increasing energy-transfer probability among the Mn²⁺ ions. The high temperature-dependent PL spectra of CCCP:10%Mn are shown in Fig. S5a (ESI).† The PL intensity monotonously decreases due to thermal-quenching. However, it still maintains 61.3% of the initial intensity at 523 K, indicating the good luminescence thermal stability of Mn²⁺ in the CCCP crystals. Meanwhile, the emission peak appears as a notable blue shift, and the full width at half maximum (FWHM) is broadened significantly. These results were caused by the intensified electron–phonon coupling effect with the increasing of the temperature. To quantify the electron–phonon interaction, temperature-dependent FWHM is usually fitted by the following eqn (3):⁴⁷

$$\text{FWHM} = 2.36 \times \hbar\omega \times \sqrt{S} \times \sqrt{\coth\left(\frac{\hbar\omega}{2kT}\right)} \quad (3)$$

where $\hbar\omega$ is the phonon frequency, S is Huang–Rhys factor, and k is the Boltzmann constant. As the fitted results in Fig. S5b (ESI)† show, the $\hbar\omega$ and S were determined to be 36.3 meV and 6, respectively. The large S implied that there was a relatively strong electron–phonon coupling effect. Based on the results presented previously, a schematic energy level diagram was constructed to illustrate the photophysical mechanism occurring in the CCCP:Mn crystals (see Fig. 2d). Upon UV light excitation, electrons can be pumped to the excited states of the CCCP host and then relax to the self-trapped states *via* non-radiative transitions, followed by the STEs emission with a large Stokes' shift. As the Mn²⁺ ions were incorporated into the CCCP host lattice, the isolated Mn²⁺ ions located in the [MnCl₆]^{4−} octahedrons can act as exciton acceptors, in addition to the self-excitation to higher energy levels, and further as the emission centres to give the strong orange PL *via* the ⁴T_{1g} to ⁶A_{1g} energy level transitions. Further doping of Mn²⁺ ions leads to the formation of the Mn²⁺–Mn²⁺ dimers, causing the exchange coupling of the energy levels. Specifically, the ground state [⁶A₁(⁶S)⁶A₁(⁶S)] was formed by

exchange coupling of the ground states of the two Mn²⁺ ions in a Mn²⁺–Mn²⁺ dimer and the lowest excited state arose from the exchange coupling between the first excited state of one Mn²⁺ [⁴T₁(⁴G)] and the ground state of another Mn²⁺ [⁶A₁(⁶S)] in a Mn²⁺–Mn²⁺ dimer. Consequently, the exchange coupling resulted in a red-shifted orange emission from the Mn²⁺–Mn²⁺ dimers.

Apart from the orange emission, more interesting is the observation of a long orange afterglow in both the pristine and Mn²⁺-doped CCCP crystals after UV irradiation (Fig. 3a and ESI†). From the afterglow decay curves shown in Fig. 3b, it can be seen that the afterglow was greatly enhanced by Mn²⁺ doping and approached its optimum at $x = 2$. To determine the trap effect on afterglow, the TL curves of CCCP: $x\%$ Mn crystals were measured at a heating rate of 2 °C s^{−1} after 254 nm UV light irradiation. As shown in Fig. 3c, the CCCP: $x\%$ Mn crystals exhibited TL curves with a broad band from 30 to 300 °C with apparent two peaks, which indicating a complex trap distribution. As the Mn²⁺ doping concentration increased, the TL intensity increased initially, reaching a maximum at $x = 2$, and then decreased, which indicated that the incorporation of Mn²⁺ induced the enrichment of the traps. To reveal the contributions of different traps to the orange afterglow, the TL

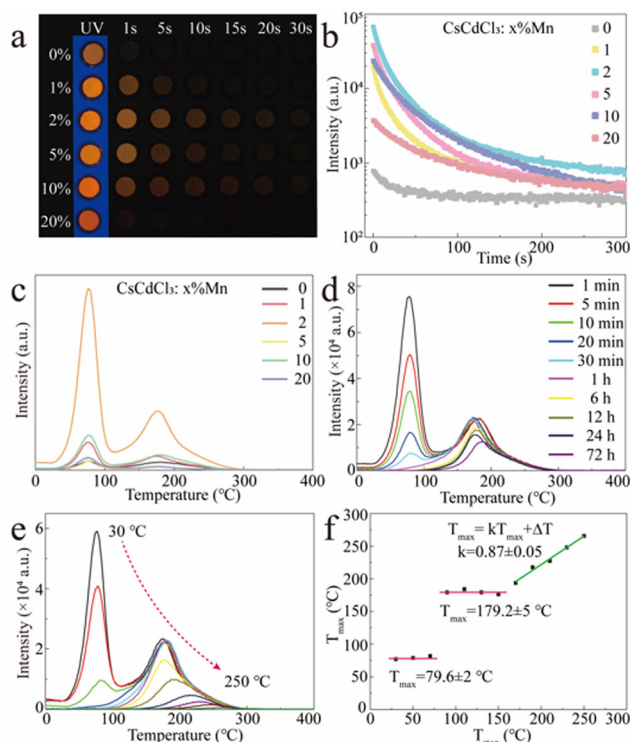


Fig. 3 (a) Afterglow photographs of CCCP: $x\%$ Mn ($x = 0$ –20) crystals taken under UV excitation and at different times after the removal of the UV light. (b) Afterglow decay curves, and (c) TL curves of CCCP: $x\%$ Mn ($x = 0$ –20). (d) The TL curves of CCCP:2%Mn obtained at various delay times from 1 min to 24 h. (e) The TL curves of CCCP:2%Mn recorded with preheating at various temperatures. (f) The $T_{\text{max}} - T_{\text{stop}}$ plot of CCCP:2%Mn.

glow curves were recorded at different delay times and these are shown in Fig. 3d. It was evident that the intensity of the low-temperature TL declined rapidly and almost disappeared after 6 h but for the high temperature TL one this was very slow (more than 50% intensity remained after 72 h decay), which indicated that the observable orange afterglow was mainly dominated by the easier release of electrons from shallow traps with a smaller energy barrier. The deep traps with a much higher energy barrier meant that it was difficult to release the trapped electrons, resulting in the almost unnoticeable afterglow at room temperature. When the thermal field was applied, the nearly frozen electrons were endowed with a higher energy and were then impelled promptly to escape out of the deep traps, causing a bright orange emission. As shown in Fig. 3e, to further extract the trap distribution in the Mn^{2+} -doped CCCP crystals, the TL curves were measured using a thermal cleaning method devised by McKeever.^{48,49} As expected, the low-temperature TL peak drops sharply and the high-temperature TL peak shifts gradually to the higher temperature side as the preheating temperature is increased from 30 to 250 °C, which arose from the thermally stimulated electrons from the traps to the emission centres. From these results, the relationship of $T_{\text{max}}-T_{\text{stop}}$ (T_{max} : the temperature of the TL peak maximum at the low-temperature side, T_{stop} : the preheating temperature) was drawn and is shown in Fig. 3f. The $T_{\text{max}} - T_{\text{stop}}$ plot exhibits three distinct intervals: two flat platforms at about 79.6 ± 2 and 179.2 ± 5 °C at the lower T_{stop} ranges, and an oblique stage at the higher T_{stop} . The two flat platforms were independent of the preheating temperature which implied the presence of two individual discrete trap energy levels. The gradual increase of T_{max} with the increasing preheating temperatures in the oblique stage indicated the existence of a continuous trap distribution. Thus, it can be concluded that the low-temperature TL peak is mainly attributed to a single discrete trap which dominates the observable orange afterglow, whereas the high-temperature TL peak is overlapped with a single discrete trap and continuously distributed traps. The trap depth (E_{trap}) is usually estimated by the following formula:³¹

$$E_{\text{trap}} = T_{\text{max}}/500 \quad (4)$$

Accordingly, the trap depths were estimated to be 0.71 and 0.90 eV for the two individual discrete traps, as well as 0.90–1.08 eV for the continuously distributed traps.

Although the excited orange afterglow was observed in Mn^{2+} -doped CCC MHP crystals, the afterglow performance still needed to be improved due to the limited filling ability (the traps seemingly reached saturation just by using UV irradiation at 254 nm for 30 s as shown in Fig. S6 (ESI)[†]) and the application is to be expanded. Keeping this in mind, we attempted to use X-rays alone as the excitation source. The TL intensity was much stronger than the UV irradiated one and the traps reached a saturation until the X-ray irradiation for 1 min occurred (Fig. S7, ESI[†]). As shown in Fig. 4a, the orange afterglow of CCCP:2%Mn²⁺ is greatly prolonged from ~70 min by UV excitation to ~300 min by X-ray irradiation, which is

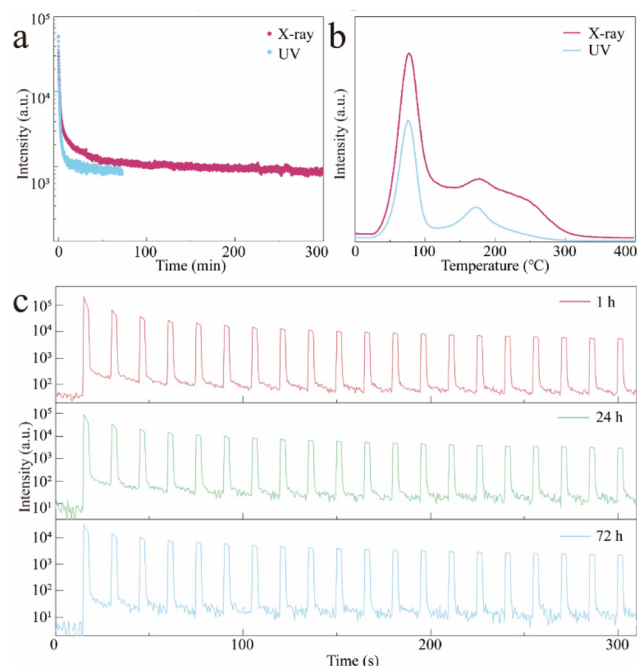


Fig. 4 (a) Afterglow decay curves, and (b) the TL glow curves of CCCP:2%Mn²⁺ after excitation by 254 nm UV light and X-rays for 10 min. (c) The repeated OSL obtained at different decay times (1, 24, and 72 h) with an 870 nm NIR light stimulus. The stimulation time in each cycle was set as 3 s.

caused by the stronger filling capability of high-energy X-ray. As shown in Fig. 4b, the overall TL intensity of CCCP:2%Mn²⁺ with irradiation was much stronger than that with UV light irradiation, confirming that the X-rays may be a powerful tool, inducing more effective trap filling, thus triggering a better afterglow performance. In addition to the self-release of the trapped electrons at RT, and the thermally-facilitated electron release at high temperature, the localized electrons can also be stimulated from traps to Mn²⁺ emission centres, causing OSL.⁵⁰ As shown in Fig. 4c, repeated OSL curves were obtained at different decay times (1, 24, and 72 h) using a 870 nm NIR light stimulus. After 72 h of decay after the stoppage of X-ray irradiation, the orange afterglow which had almost disappeared could still can be rejuvenated several times to a strong intensity and it showed very slight attenuation of the light intensity after 20 cycles of testing. It allows the as-obtained CCCP:Mn scintillator to be used for the on-demand and late-time detection of X-ray images.

As a proof-of-concept, the as-obtained CCCP:2%Mn²⁺ was prepared in the form a flexible phosphor film with a diameter of 6 cm for the scintillator screen (see the inset of Fig. 5a). The RL spectrum (Fig. 5a) of the scintillator film exhibited the same shape as the emission spectrum (Fig. 2b), which implied the occurrence of orange RL. Fig. 5b shows a schematic diagram of the real-time online and time-lapse offline X-ray imaging systems employing the scintillator film. In the former case, the image can be taken using an ordinary digital camera or a mobile phone after being reflected 45 degrees by a flat

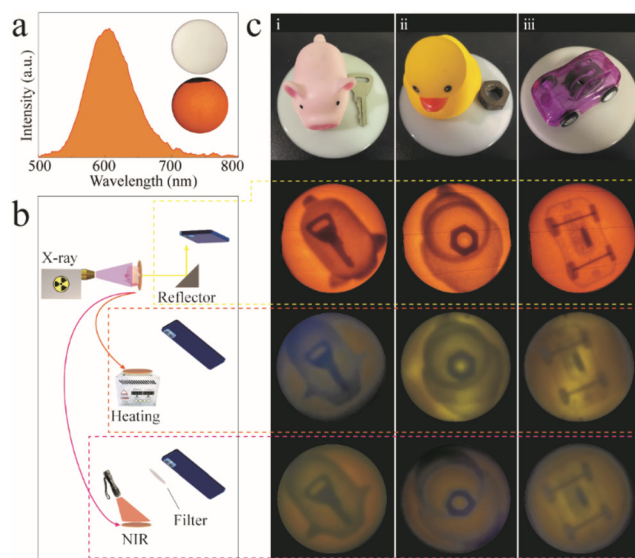


Fig. 5 (a) The RL spectrum of the fabricated phosphor film. Inset: photographs of the film under daylight (top) and X-ray irradiation (bottom). (b) The schematic diagram of the real-time and time-lapse (with external heating and NIR light stimuli) X-ray imaging. (c) The real-time and time-lapse X-ray imaging photographs of various objects, including a key inside a rubber pig (i), a nut inside a rubber duck (ii), and a plastic toy car (iii), under daylight (first row), X-ray irradiation (second row), and then heating (third row), and NIR light stimulus after the removal of X-ray irradiation (fourth row).

mirror, and this effectively avoids the noise signal produced by direct incident X-rays ($72.3 \text{ mGy}_{\text{air}} \text{ s}^{-1}$). In the latter case, the images were taken directly above the charged films under the thermal and light fields. To determine the spatial resolution, the modulation transfer function (MTF) calculation was carried out by using slanted-edge image. As shown in Fig. S8 (ESI),[†] the spatial resolution of 12.2 lp mm^{-1} was obtained at a MTF of 0.2. As shown in Fig. 5c, a key inside a rubber pig (i), a nut inside a rubber duck (ii), and a plastic toy car (iii) were used for the real-time and time-lapse X-ray imaging. The target objects, including the key, nut, and the internal structure of the toy car, were clearly seen without distortion (see second row in Fig. 5c), which demonstrated high resolution real-time X-ray imaging. The flexible films were able to record the patterns during the X-ray exposure, meaning that there is potential to perform time-lapse X-ray imaging. After the stoppage of the X-ray irradiation, the recorded patterns can also be visualized, and captured by applying the thermal (180°C) and light (870 nm) fields, which can be seen in the third and fourth rows in Fig. 5c. The previous results demonstrate that the CCCP:Mn²⁺ may be a potential candidate for both real-time and time-lapse X-ray imaging.

4. Conclusions

In conclusion, we have synthesized, all-inorganic hexagonal cadmium-based MHP crystals combining the scintillation and

afterglow properties *via* a typical hydrothermal method. The incorporation of Mn²⁺ resulted in the $^4\text{T}_{1\text{g}}$ to $^6\text{A}_{1\text{g}}$ transitions with an intense orange emission, which was 11.3 times stronger than the pristine STE emission from the non-doped CCCP crystals. The red shift of the Mn²⁺ emission with doping was attributed to the stronger interaction of Mn²⁺–Mn²⁺ dimers. The as-obtained Mn²⁺-doped CCCP crystals could be excited by X-rays and were capable of producing excellent orange long afterglows lasting over 300 min. Moreover, the structure and property relationships, encompassing PL, afterglow, OSL, and scintillation properties, were comprehensively investigated. By virtue of the exceptional X-ray absorption capacity and long afterglow features, flexible scintillator films were manufactured using the as-obtained CCCP crystals to demonstrate not only the real-time online X-ray imaging with a spatial resolution of 12.2 lp mm^{-1} , but also the extended application for offline time-lapse X-ray imaging. The resulting insights will be used to design and optimize new MHPs for advanced offline X-ray imaging applications.

Author contributions

Sijian Wu: conceptualization, methodology, investigation, writing – original draft, writing – review, and writing – editing. Lifang Yuan: conceptualization, investigation, and data curation. Geng Chen: software and validation. Chaoyue Peng: validation and investigation. Yahong Jin: writing – review, writing – editing, supervision, data curation, and funding acquisition.

Conflicts of interest

There are no conflicts to declare.

Acknowledgements

This work was supported by the National Natural Science Foundation of China (Grant No. 51802045) and a Guangzhou Basic and Applied Basic Research Project (Grant No. 202102020871). The authors would also like to thank the staff of the Analysis and Test Center of Guangdong University of Technology for their help with the XRD and diffuse reflectance spectroscopy analyses.

References

- 1 Y. Zhou, J. Chen, O. M. Bakr and O. F. Mohammed, *ACS Energy Lett.*, 2021, **6**, 739–768.
- 2 F. Zhou, Z. Li, W. Lan, Q. Wang, L. Ding and Z. Jin, *Small Methods*, 2020, **4**, 2000506.
- 3 H. Wu, Y. Ge, G. Niu and J. Tang, *Matter*, 2021, **4**, 144–163.
- 4 M. da C. C. Pereira, T. M. Filho, J. R. Berretta and C. H. de Mesquita, *Mater. Sci. Appl.*, 2018, **9**, 268.

- 5 W. Mengesha, T. Taulbee, B. Rooney and J. Valentine, *IEEE Trans. Nucl. Sci.*, 1998, **45**, 456–461.
- 6 K. Takagi, T. Ooi, T. Fukazawa, M. Ishii and S. Akiyama, *J. Cryst. Growth*, 1981, **52**, 584–587.
- 7 J. Mares, M. Nikl, N. Solovieva, C. D'Ambrosio, F. De Notaristefani, K. Blazek, P. Maly, K. Nejezchleb, P. Fabeni and G. Pazzi, *Nucl. Instrum. Methods Phys. Res., Sect. A*, 2003, **498**, 312–327.
- 8 K. Han, J. Jin, B. Su, J. Qiao and Z. Xia, *Adv. Opt. Mater.*, 2022, **9**, 3529–3539.
- 9 Z. Xu, X. Liu, Y. Li, X. Liu, T. Yang, C. Ji, S. Han, Y. Xu, J. Luo and Z. Sun, *Angew. Chem., Int. Ed.*, 2019, **58**, 15757.
- 10 J. Jin, K. Han, Y. Hu and Z. Xia, *Adv. Opt. Mater.*, 2023, 2300330.
- 11 K. Han, K. Sakhatskyi, J. Jin, Q. Zhang, M. V. Kovalenko and Z. Xia, *Adv. Mater.*, 2022, **34**, 2110420.
- 12 Q. Chen, J. Wu, X. Ou, B. Huang, J. Almutlaq, A. A. Zhumeckenov, X. Guan, S. Han, L. Liang, Z. Yi, J. Li, X. Xie, Y. Wang, Y. Li, D. Fan, D. B. L. Teh, A. H. All, O. F. Mohammed, O. M. Bakr, T. Wu, M. Bettinelli, H. Yang, W. Huang and X. Liu, *Nature*, 2018, **561**, 88–93.
- 13 J. H. Heo, D. H. Shin, J. K. Park, D. H. Kim, S. J. Lee and S. H. Im, *Adv. Mater.*, 2018, **30**, 1801743.
- 14 H. Zhang, Z. Yang, M. Zhou, L. Zhao, T. Jiang, H. Yang, X. Yu, J. Qiu, Y. Yang and X. Xu, *Adv. Mater.*, 2021, **33**, 2102529.
- 15 L. Han, H. Zhang, Y. Ning, H. Chen, C. Guo, J. Cui, G. Peng, Z. Ci and Z. Jin, *Chem. Eng. J.*, 2022, **430**, 132826.
- 16 Q. Zhou, J. Ren, J. Xiao, L. Lei, F. Liao, H. Di, C. Wang, L. Yang, Q. Chen, X. Yang, Y. Zhao and X. Han, *Nanoscale*, 2021, **13**, 19894–19902.
- 17 L. Lian, M. Zheng, W. Zhang, L. Yin, X. Du, P. Zhang, X. Zhang, J. Gao, D. Zhang, L. Gao, G. Niu, H. Song, R. Chen, X. Lan, J. Tang and J. Zhang, *Adv. Sci.*, 2020, **7**, 2000195.
- 18 T. He, Y. Zhou, X. Wang, J. Yin, L. Gutiérrez-Arzaluz, J.-X. Wang, Y. Zhang, O. M. Bakr and O. F. Mohammed, *ACS Energy Lett.*, 2022, **7**, 2753–2760.
- 19 F. Zhang, Y. Zhou, Z. Chen, M. Wang, Z. Ma, X. Chen, M. Jia, D. Wu, J. Xiao and X. Li, *Adv. Mater.*, 2022, **34**, 2204801.
- 20 S. He, Q. Qiang, T. Lang, M. Cai, T. Han, H. You, L. Peng, S. Cao, B. Liu and X. Jing, *Angew. Chem.*, 2022, **134**, e202208937.
- 21 Z. Tang, R. Liu, J. Chen, D. Zheng, P. Zhou, S. Liu, T. Bai, K. Zheng, K. Han and B. Yang, *Angew. Chem., Int. Ed.*, 2022, **61**, e202210975.
- 22 S. Wu, L. Yuan, G. Chen, Z. Li and Y. Jin, *J. Lumin.*, 2022, **252**, 119374.
- 23 V. Shanker, D. Haranath and G. Swati, *Defect Diffus. Forum*, 2015, **361**, 69–94.
- 24 S. Xu, R. Chen, C. Zheng and W. Huang, *Adv. Mater.*, 2016, **28**, 9920–9940.
- 25 M. Li, Y. Jin, L. Yuan, B. Wang, H. Wu, Y. Hu and F. Wang, *ACS Appl. Mater. Interfaces*, 2023, **15**, 13186–13194.
- 26 B. Wang, H. Wang, J. Huang, J. Zhou and P. Liu, *J. Am. Ceram. Soc.*, 2019, **103**, 315–323.
- 27 B.-M. Liu, R. Zou, S.-Q. Lou, Y.-F. Gao, L. Ma, K.-L. Wong and J. Wang, *Chem. Eng. J.*, 2021, **404**, 127133.
- 28 T. Lyu, P. Dorenbos, C. Li, S. Li, J. Xu and Z. Wei, *Chem. Eng. J.*, 2022, **435**, 135038.
- 29 X. Zhou, K. Han, Y. Wang, J. Jin, S. Jiang, Q. Zhang and Z. Xia, *Adv. Mater.*, 2023, **35**, 2212022.
- 30 X. Ou, X. Qin, B. Huang, J. Zan, Q. Wu, Z. Hong, L. Xie, H. Bian, Z. Yi and X. Chen, *Nature*, 2021, **590**, 410–415.
- 31 W. Zheng, X. Li, N. Liu, S. Yan, X. Wang, X. Zhang, Y. Liu, Y. Liang, Y. Zhang and H. Liu, *Angew. Chem., Int. Ed.*, 2021, **60**, 24450–24455.
- 32 X. Wang, X. Zhang, S. Yan, H. Liu and Y. Zhang, *Angew. Chem.*, 2022, **134**, e202210853.
- 33 A. Vink, M. De Bruin, S. Roke, P. Peijzel and A. Meijerink, *J. Electrochem. Soc.*, 2001, **148**, E313.
- 34 R. D. Shannon, *Acta Crystallogr., Sect. A: Cryst. Phys., Diffraction, Theor. Gen. Crystallogr.*, 1976, **32**, 751–767.
- 35 Y. Su, L. Yuan, B. Wang, S. Wu and Y. Jin, *J. Colloid Interface Sci.*, 2022, **624**, 725–733.
- 36 G. Xiong, L. Yuan, Y. Jin, H. Wu, B. Qu, Z. Li, G. Ju, L. Chen, S. Yang and Y. Hu, *J. Mater. Chem. C*, 2021, **9**, 13474–13483.
- 37 C. F. Holder, J. Fanghanel, Y. Xiong, I. Dabo and R. E. Schaak, *Inorg. Chem.*, 2020, **59**, 11688–11694.
- 38 S. Li, J. Luo, J. Liu and J. Tang, *J. Phys. Chem. Lett.*, 2019, **10**, 1999–2007.
- 39 P. Han, C. Luo, S. Yang, Y. Yang, W. Deng and K. Han, *Angew. Chem., Int. Ed.*, 2020, **59**, 12709–12713.
- 40 B. Su, G. Zhou, J. Huang, E. Song, A. Nag and Z. Xia, *Laser Photonics Rev.*, 2021, **15**, 2000334.
- 41 J.-H. Wei, J.-F. Liao, X.-D. Wang, L. Zhou, Y. Jiang and D.-B. Kuang, *Matter*, 2020, **3**, 892–903.
- 42 Q. Wei, M. Li, Z. Zhang, J. Guo, G. Xing, T. C. Sum and W. Huang, *Nano Energy*, 2018, **51**, 704–710.
- 43 X. Li, T. Liu, K. Zhang, Z. Hu, H. An, S. Deng, Y. Kong and B. Wang, *J. Mater. Chem. C*, 2023, **11**, 712–721.
- 44 E. Song, S. Ye, T. Liu, P. Du, R. Si, X. Jing, S. Ding, M. Peng, Q. Zhang and L. Wondraczek, *Adv. Sci.*, 2015, **2**, 1500089.
- 45 K. Han, J. Qiao, S. Zhang, B. Su, B. Lou, C. Ma and Z. Xia, *Laser Photonics Rev.*, 2023, **17**, 2200458.
- 46 X. Li, W. Huang, R. Zhang, Y. Guo, H. Yang, X. He, M. Yu, L. Wang and Q. Zhang, *Rare Met.*, 2022, **41**, 1230–1238.
- 47 J. Jin, Y. Peng, Y. Xu, K. Han, A. Zhang, X.-B. Yang and Z. Xia, *Chem. Mater.*, 2022, **34**, 5717–5725.
- 48 S. W. S. McKeever, *Phys. Status Solidi A*, 1980, **62**, 331–340.
- 49 C. Wang, Y. Jin, J. Zhang, X. Li, H. Wu, R. Zhang, Q. Yao and Y. Hu, *Chem. Eng. J.*, 2023, **453**, 139558.
- 50 L. Yuan, Y. Jin, Y. Su, H. Wu, Y. Hu and S. Yang, *Laser Photonics Rev.*, 2020, **14**, 2000123.